Journal of Materials Chemistry A

ROYAL SOCIETY OF CHEMISTRY

PAPER

View Article Online
View Journal

Cite this: DOI: 10.1039/d6ta00988c

Structure-dependent electronic modulation of Pt on perovskite surfaces: bifunctional oxygen catalysts for rechargeable Zn–air batteries

Boyean Kim,[a] Kyeongwon Han,[a] Yuri Ko,[a] Chanmin Lee*[bc] and Yukwon Jeon *[a]

Received 2nd February 2026
Accepted 28th March 2026

DOI: 10.1039/d6ta00988c

rsc.li/materials-a

The Zn–air batteries (ZABs) have emerged as promising candidates for advancing energy storage systems in the transition to a clean energy society. Nevertheless, the sluggishness of the oxygen reduction/evolution reaction (ORR/OER) on the air cathode is a prevalent problem in ZABs. Herein, we designed perovskite catalysts with platinum (Pt) loading to function as an oxygen electrocatalyst for the cathode to explore the modulation of their crystal and electronic structure with the goal of enhancing their catalytic performance. Barium titanate-based manganese-doped perovskites ($BaTi_{1-x}Mn_xO_{3-\delta}$) were designed, and their structural transitions (tetragonal → hexagonal → rhombohedral) were confirmed by Rietveld refinement analysis. With a low level of deposited Pt on the surface, the structural variation of perovskite led to changes in the electronic and chemical properties of surface Pt, thereby affecting its catalytic behaviour. In particular, hexagonal Pt–$BaTi_{0.8}Mn_{0.2}O_{3-\delta}$ exhibited the co-formation of metallic Pt^0 and oxygen vacancies, which collectively promoted the O* spillover pathway during oxygen redox reactions, leading to an excellent bifunctional performance of $\Delta E = 1.02$ V. For a ZAB application, this catalyst exhibited remarkable performance, with a specific capacity of 736 mA h g^{-1} and maintained cyclic stability over 250 h and 1500 cycles, demonstrating that the electronic interactions between the perovskite and the surface Pt varies depending on the crystal structure. By proposing an efficient spillover-assisted reversible oxygen reaction mechanism, this work provides a design strategy for high-performance bifunctional electrocatalysts in ZABs.

Introduction

As demand for energy continues to increase in the context of the depletion of fossil fuels, there is an increasing need to develop sustainable electrochemical energy storage systems that are environmentally sound and cost-effective.[1,2] Rechargeable metal–air batteries (metal = Li, Zn, Al, *etc.*) possess a high theoretical energy density, which can be attributed to the utilization of ambient air as a cathode, and so reducing the weight of cathode side materials.[3,4] In this regard, Zn–air batteries (ZABs) are recognized as desirable choices because of their high theoretical energy density (1086 W h kg^{-1}), inherent safety, low cost relative to the abundant Zn resources (<US$ 10 kW^{-1} h^{-1} for ZABs *vs.* US$ 400–800 kW^{-1} h^{-1} for Li-ion batteries), and environmental friendliness.[5,6]

Recently, extensive research has focused on a wide range of elements for ZAB applications, with the intention of enhancing their efficiency.[4,7] This is due to the fact that the fundamental principles of the operation of ZABs are governed by the oxygen evolution reaction (OER) and oxygen reduction reaction (ORR) at the air cathode, which occur during charge and discharge, respectively.

It is well documented that these reactions are sluggish, which has been attributed to a four-electron transfer process, resulting in high overpotentials and low energy efficiency.[8–10] Consequently, there is a pressing need for research into effective and stable bifunctional oxygen catalysts. Noble-metal-based catalysts have been extensively employed to accelerate oxygen redox reactions, and platinum (Pt)- and iridium oxide (IrO_2)-based materials are currently used as benchmarks for ORR and OER catalysts. However, these precious metals are expensive and even unstable due to their low resistance to repeated cycles in an oxidation-reduction environment, and therefore, cost-effective and stable bifunctional oxygen catalysts are being investigated.[4]

In recent years, transition metal oxide catalysts have emerged as an abundant and cost-effective alternative for bifunctional oxygen catalysts, and they can adopt a variety of structures, including monoxide, dioxide, perovskite, and spinel

[a]*Department of Environmental and Energy Engineering, Yonsei University, 1 Yonseidae-gil, Wonju 26493, Republic of Korea. E-mail: ykjeon@yonsei.ac.kr*

[b]*Green and Sustainable Materials R&D Department, Korea Institute of Industrial Technology, 89 Yangdaegiro-gil, Ipjang-myeon, Seobuk-gu, Cheonan-si 31056, Republic of Korea. E-mail: clee@kitech.re.kr*

[c]*Department of Chemical Engineering, Chung-Ang University, Seoul 06974, Republic of Korea*

oxide, and offer enriched active sites and the flexibility for electronic modulation.[7,8]

The perovskite oxides are regarded as promising candidates due to their interesting electrocatalytic properties. Typically, perovskite oxide is structured according to the ABO_3 formula, where the A-site cations are usually occupied by alkaline earth metals or rare earth metals (La, Ba, Sr, *etc.*), and the B-site cations are occupied by 3d transition metals (Mn, Fe, Co, *etc.*).[11–13] This configuration can be flexibly regulated, and the modulation of cations is widely regarded as an effective approach to improving the electrocatalytic performance, primarily through the modulation of the electronic structure and crystal lattice.[11]

Barium titanate ($BaTiO_3$) is an inorganic perovskite material that is used in the field of multilayer ceramic capacitors (MLCCs) and thermistors due to its excellent dielectric and ferroelectric properties.[14] $BaTiO_3$-based perovskites are useful because of their tunable crystal structures.[15] Therefore, recent works have explored their application in the domain of electrochemical research, which has adapted various strategies such as A- and B-site cation doping and creating a defect for each cation and anion.[16–22]

Recently, research has been conducted on perovskite-supported metal clusters and nanoparticles, with the aim of enhancing the activity and cyclic redox stability. These have been identified as promising candidates for the ORR and OER due to their synergistic effects between the metal and the support, *e.g.*, the 'spillover effect'.[23–26] The various properties of perovskite with the supported metal affect catalytic activities, including the synergies between the metal and crystal structures, the compositions of oxygen species, and the electronic structures of perovskite.

In the current study, the transition metal manganese (Mn) was doped into the B-site of $BaTiO_3$ ($BaTi_{1-x}Mn_xO_{3-\delta}$, $x = 0$, 0.2, 0.4, 0.6) perovskite. The structural transition of $BaTi_{1-x}Mn_xO_{3-\delta}$ (BTM*x*) perovskites has been the subject of extensive research due to the various crystal structures they can assume by changing the doping amount of Mn. However, the structural transition mechanisms leading to catalytic activity for the ORR and OER have not been studied in detail.[27] In addition, the synergistic effects arising from low Pt loading and the distinct crystal structures of BTM*x* were systematically investigated as a bifunctional oxygen catalyst exhibiting efficient and stable performances, aiming to enhance the overall electrochemical behaviour of rechargeable ZABs.

Experimental section

Materials

The materials used in this work were barium carbonate ($BaCO_3$, 99% Sigma-Aldrich), titanium oxide (TiO_2, 99.8% Sigma-Aldrich), manganese oxide (Mn_3O_4, 97% Sigma-Aldrich), platinum chloride ($PtCl_2$, 98% Sigma-Aldrich), iridium oxide (IrO_2, 99.9% Sigma-Aldrich), 20 wt% Pt on Vulcan XC-72R (Pt/C, Premetek), KOH (ACS reagent, 85% pellet Sigma-Aldrich), Nafion ionomer solution (5 wt% Chemours), Zn sheet (99.99% Nilaco), carbon paper (AvCarb P75T, Fuel Cell Store), Ni mesh (100 mesh Nilaco), and a separator membrane (Celgard® 3501).

Catalyst preparation

$BaTi_{1-x}Mn_xO_{3-\delta}$, where perovskite oxides with $x = 0$, 0.2, 0.4, and 0.6 are denoted as BTO, BTM2, BTM4, and BTM6, respectively, was synthesized by a conventional solid-state method. Stoichiometric amounts of $BaCO_3$, TiO_2, and Mn_3O_4 precursors were mixed with acetone and stirred for 12 h to obtain a homogeneous mixture. The resulting powders were calcined at 1000 °C for 12 h, and then ground in an algae mortar and pelletized. Finally, the pellets were sintered at 1400 °C for 12 h. The 5 wt% Pt-loaded BTM*x* (Pt-BTM*x*) catalysts were prepared by an impregnation method, denoted as Pt-BTM2, Pt-BTM4, and Pt-BTM6. The corresponding amounts of $PtCl_2$ and pre-synthesized BTM*x* were mixed with acetone for 12 h. The dried powders were calcined at 300 °C for 2 h. All heat treatments were carried out in an open atmosphere.

Material characterization

The powder X-ray diffraction (PXRD) data for each catalyst were collected using a D2 Phaser (Bruker AXS) at room temperature with an X-ray angle in the range 20–80°. The X-ray source used was Cu Kα ($\lambda = 1.5418$ Å), and Rietveld refinement was conducted to determine the lattice parameters and structure of the perovskites using the FullProf Suite program. The transmission electron microscopy (TEM) and energy-dispersive spectroscopy (EDS) measurements were carried out on JEM-ARM 200F NEOARM (JEOL, Tokyo, Japan). X-ray photoelectron spectroscopy (XPS) was carried out using a K-Alpha XPS system (Thermo VG, UK). The obtained XPS spectra were deconvoluted and fitted using Fityk software.

Electrochemical activity measurement

A rotating disk electrode (RDE) system using an RDE710 rotating electrode (Gamry Instruments, USA) was used to characterize the electrochemical catalytic activities of the developed catalysts at room temperature. Pt wire, Hg/HgO (1 M NaOH), and a glassy carbon electrode (surface area of 0.196 cm^2) were used as the counter, reference, and working electrodes, respectively. A uniform slurry was obtained by mixing 5 mg of prepared catalyst and 25 mg of Vulcan XC-72 carbon with 100 μL of Nafion ionomer solution and 1.0 mL absolute ethanol, followed by ultrasonication and stirring. Then, 10 μL of the slurry was dropped onto the surface of the glassy carbon electrode, with a loading amount of 0.232 mg_{cat} cm^{-2}. For comparison with a commercial catalyst (IrO_2 + Pt/C), 2.5 mg of IrO_2, 12.5 mg of 20 wt% Pt/C, and 15 mg of Vulcan XC-72 were mixed under the same conditions, maintaining a constant ratio of catalyst to activated carbon in the slurry.

The bifunctional oxygen electrocatalytic activities of the electrocatalysts were characterized by linear sweep voltammetry (LSV) at a scan rate 5 mV s^{-1} in O_2-saturated 0.1 M KOH solution. LSV curves of the ORR and OER were measured between 0.0–1.2 V and 1.2–2.0 V at a rotation speed of 1600 rpm. In addition, the measured electrochemical data were *iR*-

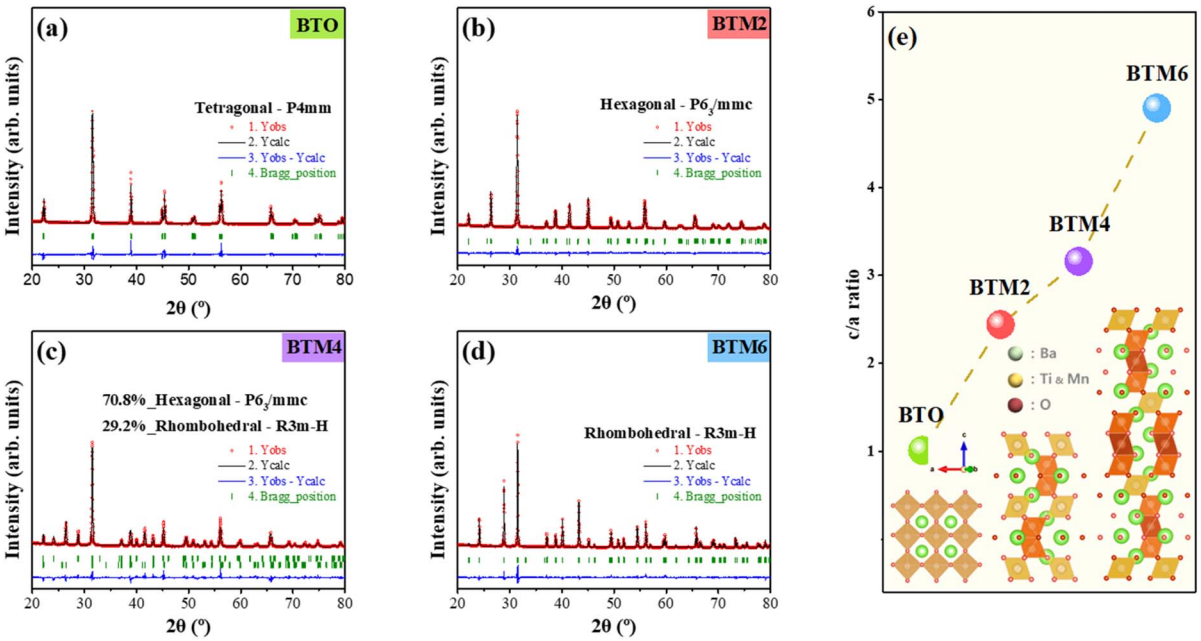

Fig. 1 Crystal structure of catalysts, and Rietveld refined XRD patterns of (a) BTO, (b) BTM2, (c) BTM4, and (d) BTM6. The red dots represent the observed data, black and blue lines represent the calculated pattern and the difference of observed and calculated, respectively, and the green vertical line represents the Bragg positions. (e) The *c*/*a* ratio of each catalyst and structural model; each coloured polyhedron is filled with a unique position of B-site metal (Ti, Mn).

compensated to eliminate the influence of solution resistance ($R_s \simeq 45\ \Omega$). Finally, the electrode potential was converted to the reversible hydrogen electrode (RHE). The electrochemical impedance spectroscopy (EIS) measurements were conducted at 0.7 V and 1.7 V *vs.* RHE under an amplitude of 10 mV from 100 kHz to 0.01 Hz. The electron transfer number (n) was calculated by Koutecky–Levich (K–L) plots obtained from the LSV curves, which were performed using different rotation speeds, from 400 rpm to 2400 rpm, and calculated using the following eqn (1) and (2):

$$\frac{1}{J} = \frac{1}{J_k} + \frac{1}{B\omega^{1/2}} \quad (1)$$

$$B = 0.62nFC_{O_2}D_{O_2}^{2/3}\gamma^{-1/6} \quad (2)$$

where J and J_k represent the measured current and kinetic current, respectively, and the rotation speed is denoted as ω in eqn (1). The slope of K–L 'B' was determined using eqn (2), where n denotes the number of electrons gained per oxygen, F denotes the Faraday constant ($F = 96\,485$ C mol^{-1}), C_{O_2} denotes the concentration of oxygen of 0.1 M KOH ($C_{O_2} = 1.26 \times 10^{-6}$ mol cm^{-3}), and D_{O2} denotes the diffusion coefficient of oxygen of 0.1 M KOH ($D_{O_2} = 1.98 \times 10^{-5}$ cm^2 s^{-1}, and kinematic viscosity ($\gamma = 0.01$ cm^2 s^{-1})).

Zn–air battery measurement

The evaluation of the homemade ZABs was carried out using a VMP-300 potentiostat (Biologic, France) at room temperature. The air cathode was constructed of commercial (IrO_2 + Pt/C) catalysts. To obtain well-dispersed ink, 5 mg of Pt-BTM*x* catalyst and 25 mg of Vulcan XC-72 carbon were mixed with 0.1 mL of Nafion ionomer solution and 5.0 mL of absolute ethanol, followed by ultrasonication at 1 h. For the comparison with the commercial catalyst, 2.5 mg of IrO_2, 12.5 mg of 20 wt% Pt/C, and 15 mg of Vulcan XC-72 were mixed under the same conditions, with a constant ratio of catalyst to activated carbon in the ink. The ink was then sprayed on the one waterproof facet of carbon paper (1 mg$_{cat}$ cm^{-2}) and dried for 30 min in an oven. The catalyst-coated carbon paper and Zn sheet, which served as the air cathode and anode, respectively, were attached to the homemade ZABs. The Ni mesh and separator membrane were used as a current collector and separator, respectively. The assembled ZAB cells were filled with 6 M KOH solution as an electrolyte.

After fabricating the ZAB cells, the galvanostatic charge and discharge polarization curves were tested by a potential range of the OCV from 3.0 V to 0.0 V. The EIS measurements were performed in the frequency range of 100 kHz to 0.01 Hz at 1.0 V, and each resistance value was calculated using an equivalent circuit model created by EC-Lab software. The specific capacity of the catalyst was tested under −25 mA cm^{-2} and −10 mA cm^{-2} of current and calculated by the reduced weight of the anode metal (Zn). Then, the galvanostatic charge–discharge cycling was tested by each process per 30 min (long-term, 1 h per cycle) and each process per 5 min (short-term, 10 min per cycle) under 10 and −10 mA cm^{-2} of current. For analysis of the cyclic efficiency and stability of the ZABs, round-trip efficiency (RTE) ($E_{discharge}/E_{charge}$) was further calculated.

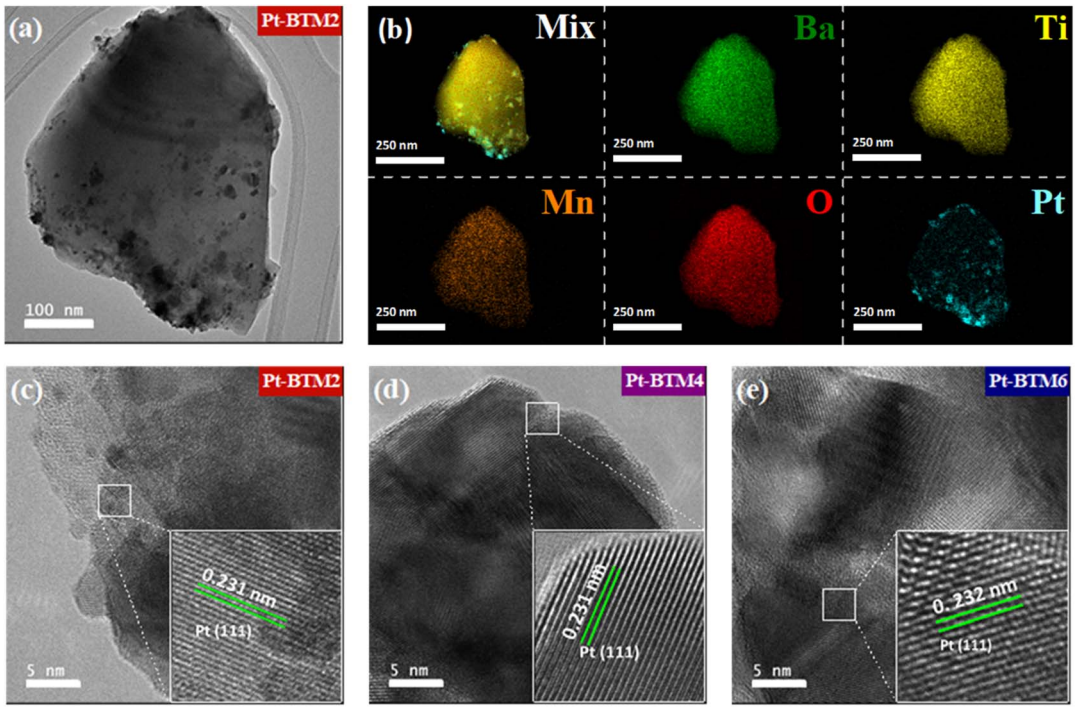

Fig. 2 TEM image of (a) Pt-BTM2 and (b) EDS chemical mapping of elements; Ba, Ti, Mn, O, and Pt. HRTEM images and lattice fringe images of Pt-loaded catalysts: (c) Pt-BTM2, (d) Pt-BTM4, and (e) Pt-BTM6.

Results and discussion

Physical structure characterization

The structural transition of each perovskite material, induced by the increasing substitution of Mn to the B-site, was confirmed using XRD and Rietveld refinement, as shown in Fig. 1. The raw XRD patterns of BTM*x* and Pt-BTM*x* are presented in Fig. S1, which show no significant changes influenced by Pt loading. Table S1 presents the detailed structural refinement data (space group, lattice parameters, and refined parameters).

It is evident from the analysis that there is a gradual transition in the crystal structure of perovskites, with an increase in the amount of doped Mn, through tetragonal, hexagonal, and rhombohedral phases.

Fig. 1(a) shows the typical tetragonal ($P4mm$) structure of $BaTiO_3$. As demonstrated in Fig. 1(b), the refined pattern of BTM2 exhibits the initial complete transition of the crystal structure to hexagonal ($P6_3/mmc$). The primary peaks of the hexagonal structure are observed at $2\theta = 22.0°$ and 26.3°, corresponding to (102) and (103) reflections, respectively. However, in Fig. 1(c), BTM4 exhibits additional peaks at $2\theta = 24.0°$ and 28.7° except the hexagonal peaks, which closely correspond to the observed rhombohedral peaks of (015) and (107) reflections, respectively. This refined data indicates that BTM4 is composed of a mixed-phase with hexagonal and rhombohedral structure at 70.8% and 29.2%, respectively. Fig. 1(d) shows the refined pattern of BTM6, indicating the second complete transition of the crystal structure, from hexagonal to rhombohedral ($R\bar{3}mH$).

The primary peaks of the rhombohedral structure were observed at $2\theta = 24.1°$ and 28.8°, and correspond to (015) and (107) reflections.

As presented in Table S1, the lattice parameters of each structure were determined as follows: for the tetragonal, $a \simeq 3.9937$ Å, $c \simeq 4.0347$ Å; for the hexagonal, $a \simeq 5.6996$ Å, $c \simeq 13.9180$ Å; and for the rhombohedral, $a \simeq 5.6778$ Å, $c \simeq 27.8528$ Å. Notably, each crystal structure exhibits a substantial variation in the *c*-axis lattice parameter. The calculated ratio of the *c*/*a* lattice length and its structural models are shown in Fig. 1(e). The increase in Mn doping is proportional to the expansion of the lattice along the *c*-axis within a single unit cell, which is related to the oxidation states of Mn. It has been established that the excess low-valent Mn ions are unable to dissolve in the hexagonal structure, and they transfer to a high-valent form in the long rhombohedral structure.[28] This suggests that the hexagonal structure of BTM2 and BTM4 contains Mn^{2+}/Mn^{3+}, and the rhombohedral structure of BTM4 and BTM6 maintains Mn^{3+}/Mn^{4+} dominance over the hexagonal structure.

To obtain structural and compositional information regarding surface Pt-loaded catalysts, TEM and EDS chemical mapping analysis were conducted. The corresponding EDS profiles verified that the elemental compositions match the intended Ti/Mn ratio of the Pt-BTM*x* series, as summarized in Table S2. Although the surface Pt loading was slightly overestimated compared to the target value of 5 wt%, which was likely due to the localized nature of the sampling area and inherent inaccuracy in quantifying the light element of oxygen, all Pt-BTM*x* samples exhibited consistent ratios, allowing for a reasonable comparison of their electrochemical properties.

In Fig. 2(a), a high-magnification TEM image also reveals a uniform distribution of Pt nanoparticles (NPs) on the BTM2 surface, with a size of 6–20 nm. The EDS chemical mapping image in Fig. 2(b) further confirms that Pt NPs were uniformly dispersed onto the surface of the crystalline perovskite. Similarly, the TEM and EDS chemical mapping images of Pt-BTM4 and Pt-BTM6 show that both were also successfully synthesised with uniform surface Pt NPs in a similar size range of 10–23 nm (Fig. S2).

In terms of physical analysis, Fig. 2(c–e) display the HR-TEM analysis to investigate the crystalline lattices of the loaded Pt NPs on the Pt-BTM*x* surfaces. Although the perovskite lattice was difficult to detect due to the high coverage of Pt species, it was observed that there was no substantial influence of the different perovskite crystal structures on the characteristics of the surface-loaded Pt. It was clearly observed that the surface lattice fringes of the Pt NPs exhibited an interplanar spacing of approximately 0.23 nm, which corresponded to the (111) diffraction plane, indicating the formation of a well-defined metallic phase.

Chemical structure characterization

The chemical bonding structures of the perovskites were analysed using XPS, as shown in Fig. 3. From the whole range survey spectra of BTM2 and Pt-BTM*x*, each catalyst spectrum demonstrates the presence of Ti 2p, Mn 2p, O 1s, and in the case of Pt-BTM*x*, Pt 4f, as expected (Fig. S3). The relative concentrations of all species were calculated through peaks fitted to specific ratios (Table S3). Upon closer examination, the high-resolution spectra of Ti 2p in Fig. 3(a) show the deconvoluted two major peaks of Ti $2p_{1/2}$ and Ti $2p_{3/2}$, which were fitted to Ti^{4+} (approximately 463.8 eV and 458.1 eV). It is evident that Pt-BTM*x* exhibited a similar position and proportion of Ti 2p, even at BTM2 (Fig. S4(a)), thereby signifying that Ti constitutes the most stable component within each crystal structure, despite the increasing Mn in the lattice.

As shown in Fig. 3(b), the high-resolution spectra of Mn 2p demonstrate the deconvoluted two major peaks Mn $2p_{1/2}$ and Mn $2p_{3/2}$, which were fitted to Mn^{2+} (approximately 652.2 eV and 640.1 eV), Mn^{3+} (approximately 653.6 eV and 642.1 eV), and Mn^{4+} (approximately 655.6 eV and 644.6 eV),[29,30] respectively. As expected, the peak intensity increased with increasing Mn doping. Moreover, the oxidation state of Mn tended to increase with higher Mn content, which was accompanied by a structural transition from the hexagonal to the rhombohedral phase. Pt-BTM2 exhibited a lower valence of Mn similar to that of the pristine BTM2 (Fig. S4(b)). In contrast, Pt-BTM4 and Pt-BTM6 exhibited higher Mn valence states, with only Mn^{3+}/Mn^{4+} peaks being fitted. This finding suggests that the surface-loaded Pt would not result in a change in the electronic structure of Mn, while the oxidation of Mn is primarily influenced by the transition of crystal structure.

In Fig. 3(c), the high-resolution spectra of O 1s demonstrate three major deconvoluted peaks, which were fitted by hydroxyl groups or absorbed oxygen (O_2/OH^-: approximately 532.4 eV), surface oxidative oxygen (O_2^{2-}/O^-: approximately 530.6 eV), and lattice oxygen (O_{Lat}: approximately 529.3 eV).[31] It has been reported that O_2^{2-}/O^- surface components are helpful in surface kinetics and assist in favouring the oxygen reactions.[27] The hexagonal structure of Pt-BTM2 contains the highest proportion of O_2^{2-}/O^- among the oxygen components. Conversely, the rhombohedral-structured Pt-BTM6 exhibited the highest

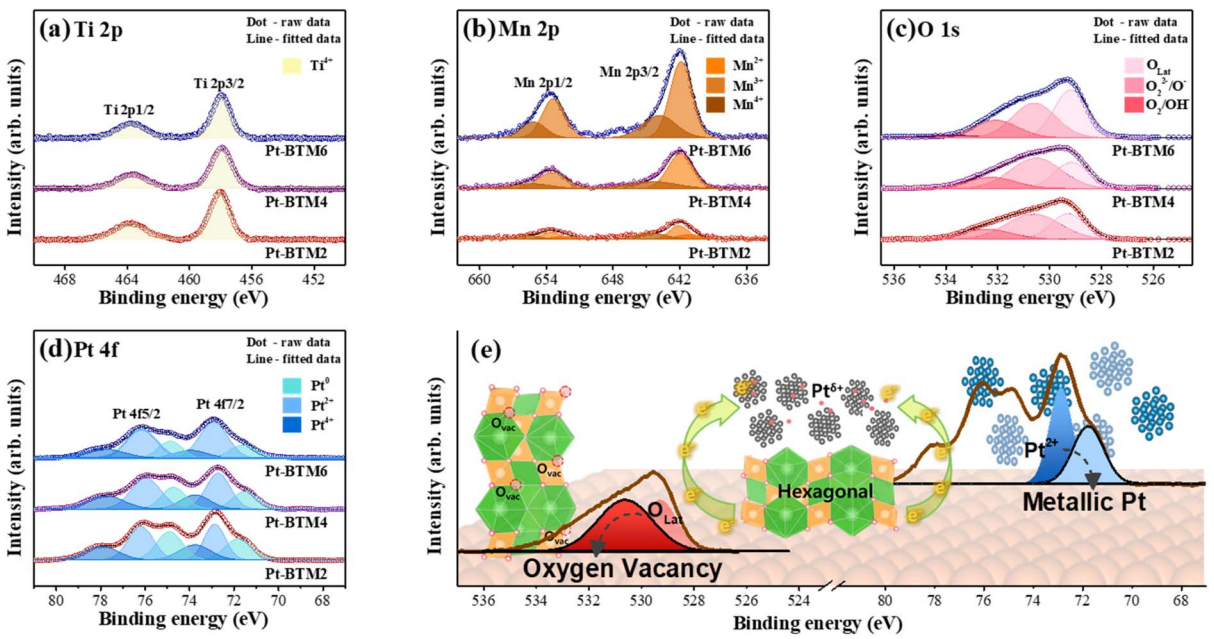

Fig. 3 High-resolution XPS spectra of Pt-BTM*x* catalysts and fitted data for each species of (a) Ti 2p, (b) Mn 2p, (c) O 1s, and (d) Pt 4f with distinguished colours corresponding to their chemical states and their relative concentrations. (e) Schematic image of the interaction between Pt species and oxygen species by electronic exchange at the hexagonal perovskite.

proportion of O_{Lat}. Interestingly, as shown in Fig. S4(c), pristine BTM2 exhibited the highest proportion of O_{Lat}. Upon Pt loading, a noticeable positive shift in the O 1s peaks was accompanied by a significant increase in the O_2^{2-}/O^- species, indicating a dramatic change in the electronic structure that was likely due to strong interactions between Pt and BTM2, and mainly facilitated through surface oxygen species.[32]

To investigate this interaction of Pt and oxygen species, Fig. 3(d) reveals the high-resolution Pt 4f XPS analysis. The Pt 4f spectra is deconvoluted into two major peaks of $4f_{5/2}$ and Pt $4f_{7/2}$, which are fitted Pt^0 (approximately 75.1 eV and 72.1 eV), Pt^{2+} (approximately 76.3 eV and 73.0 eV), and Pt^{4+} (approximately 77.8 eV and 74.1 eV).[26] Despite the synthesis and preparation conditions being equivalent, the ratio of Pt components differed between all Pt-BTM*x*. It is evident that the Pt^{4+} portion demonstrated notable similarity; however, the Pt^{2+} and Pt^0 portions exhibited distinct structural disparities. Pt-BTM2 demonstrated the highest ratio of Pt^0 among the Pt-BTM*x*. The ratio of Pt^0 decreased, while Pt^{2+} increased as the crystal structure changed from hexagonal to rhombohedral, exhibiting a trend similar to that of the surface oxygen behaviour observed in the O 1s spectra.

Consequently, the change in the electronic structure of Pt appears to be primarily influenced by the oxygen species rather than Mn ions, particularly in the hexagonal BTM2 structure. As depicted in Fig. 3(e), on the surface of hexagonal perovskite, oxygen components were oxidized from O_{Lat} to O_2^{2-}/O^-, with oxygen vacancies formed on perovskite, which modulated the change in surface Pt species to metallic Pt^0. Conversely, the higher portion of Pt^{2+} in Pt-BTM6 was likely caused by reduced Mn ions (Mn^{4+} to Mn^{3+}). This observation suggested that loaded Pt functions as an electron acceptor on the hexagonal BTM2 surface, whereas it acts as an electron donor on the rhombohedral BTM6 surface.

Bifunctional oxygen electrocatalytic performance

To analyze the electrochemical catalytic activities of the prepared (Pt-)BTM*x* catalysts, RDE measurements were initially carried out. As illustrated in Fig. S5(a), the ORR and OER LSV plots of BTM*x* are presented. It is well established that the typical BTO catalyst exhibits poor electrochemical properties.[16] However, the Mn-doped catalysts showed enhanced catalytic activity, particularly for the OER. These activities of the electrocatalysts are represented by the half-wave potential ($E_{1/2}$) for the ORR, and the overpotential at a current density of 10 mA cm^{-2} ($E_{10\ mA}$) for the OER.

While all BTM*x* catalysts exhibited ORR activities comparable to that of pristine BTO, with half-wave potentials of 0.64–0.66 V, it is notable that BTM2 demonstrated the lowest ORR Tafel slope of 75.4 mV dec^{-1}, indicating improved ORR kinetics, as shown in Fig. S5(b). Conversely, the OER activity progressively improved with increasing Mn-doping content, as evidenced by the decreasing overpotentials: BTO (1.80 V), BTM2 (1.76 V), BTM4 (1.75 V), and BTM6 (1.74 V). In this order, BTM6 exhibited the lowest OER Tafel slope of 159.5 mV dec^{-1}, confirming its enhanced OER kinetics, as shown in Fig. S5(c).

These results reveal a structure–activity relationship, where the hexagonal phase in BTM2 facilitates more efficient ORR kinetics, whereas the rhombohedral phase in BTM6 inherently enhances OER catalytic performance. This structure-driven trend is further maintained upon incorporating Pt, as the Pt-BTM*x* catalysts also exhibit synergistically improved catalytic activities consistent with their intrinsic ORR and OER characteristics.

Upon the incorporation of a small amount of Pt, the catalytic activity of all samples was significantly enhanced, for the OER and particularly for the ORR. The ORR LSV curves and corresponding Tafel plots of 5 wt% Pt-BTM*x* catalysts, along with the commercial IrO_2 + Pt/C benchmark, are shown in Fig. 4(a) and S6(a). To determine the ideal Pt loading, catalysts with 1, 5, and 8 wt% Pt were evaluated (Fig. S7). However, 1 wt% Pt showed insufficient bifunctional activity, while 5 and 8 wt% Pt exhibited comparable activity in the ORR and OER. Consequently, 5 wt% Pt was selected for this study.

Compared with Pt-BTM6 and Pt-BTM4, which exhibit half-wave potentials of 0.67 V and 0.69 V and Tafel slopes of 71.1 and 62.3 mV dec^{-1}, respectively, Pt-BTM2 exhibits highly improved ORR performance with an increased half-wave potential of 0.72 V and a lower Tafel slope of 58.9 mV dec^{-1}. Furthermore, the calculated mass activities (current density by weight of Pt) in Fig. 4(b) reveal that Pt-BTM2 achieved a significantly enhanced mass activity of 212.08 mA mg_{Pt}^{-1}, which is more than five times greater than that of the commercial IrO_2 + Pt/C catalyst (39.59 mA mg_{Pt}^{-1}).

Additionally, EIS measurements of BTM2, BTM6, Pt-BTM2, and Pt-BTM6 were performed at the ORR region of 0.7 V *vs.* RHE (Fig. S8(a)) to evaluate the resistance characteristics at each catalyst layer. With the constant electrolyte resistance, we found that the hexagonal catalysts exhibited lower charge-transfer resistance than the rhombohedral catalysts, as evidenced by

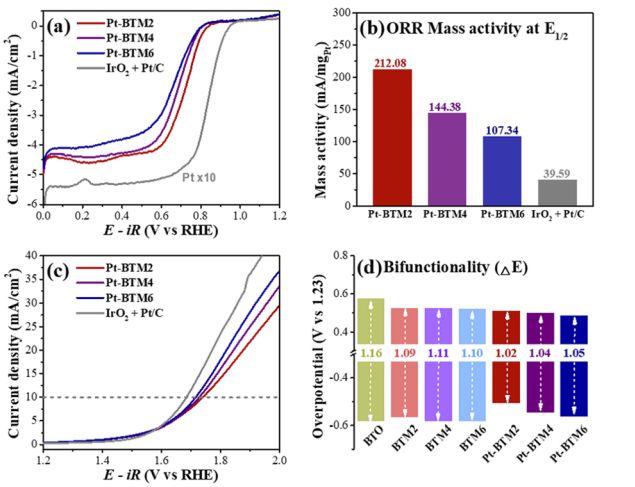

Fig. 4 Electrochemical performance of oxygen catalysts in 0.1 M KOH solution with saturated O_2 at room temperature. (a) ORR LSV plots of Pt-BTM*x* and commercial catalyst and (b) ORR mass activity obtained from (a). (c) OER LSV plots and (d) bifunctionality of oxygen catalysts.

the smaller semicircle diameters in their Nyquist plots of BTM2 *vs.* BTM6 and Pt-BTM2 *vs.* Pt-BTM6.

In addition, arguing the reaction pathway of ORR, the electron transfer numbers (n) of the pristine BTM2 and Pt-BTM2 catalysts were calculated in Fig. S9. Both revealed a first-order linear relationship between J^{-1} and $\omega^{-1/2}$, confirming the applicability of the Koutecky–Levich model. However, the calculated electron numbers were different. The overall ORR on BTM2 was found to follow a four-electron pathway, whereas Pt-BTM2 exhibited additional transferred electrons, indicating significantly improved reaction pathway efficiency by Pt incorporation. As a result, the enhanced ORR may be caused by increased metallic Pt (Pt^0) species, which strongly interact with surface oxidative oxygen components (O_2^{2-}/O^-) of the hexagonal oxide structure, thereby facilitating electron transfer with greater efficiency. It is evident that there is an additional synergistic reaction pathway between Pt and hexagonal BTM2 during the ORR process.

The OER activities of Pt-BTMx and IrO_2 + Pt/C were measured through the LSV plots and corresponding Tafel plots, respectively, in Fig. 4(c) and S6(b). In contrast to the generally recognised less effective catalytic activities of Pt in the context of the OER, it was confirmed that all Pt-BTMx catalysts demonstrated an enhancement in the OER upon Pt incorporation. In comparison to the Pt-BTMx catalysts, the Pt-BTM6 catalyst exhibited a higher catalytic activity, with a decreased overpotential of 1.72 V and a lower Tafel slope of 112 mV dec^{-1}. From the EIS spectra displayed in Fig. S8(b), the semicircle diameter of BTM6 is slightly smaller than that of BTM2. However, the difference is enlarged in the comparison after Pt deposition, where the semicircle of Pt-BTM6 is substantially reduced compared to that of Pt-BTM2. These OER results also suggest another distinct synergistic effect between ionic Pt (Pt^{2+}) and the rhombohedral perovskite lattice, which enhances charge transfer and accelerates OER kinetics.

The bifunctionality (ΔE) of the electrocatalyst, a key factor for cathode reactions in metal–air batteries, can be calculated by the potential difference between its OER and ORR activities. As illustrated in Fig. 4(d), the Mn-doped BTMx catalyst exhibited improved bifunctionality compared to the pristine BTO, which is consistent with the previously discussed structure-dependent catalytic behaviour. However, it is clear that Pt-BTMx

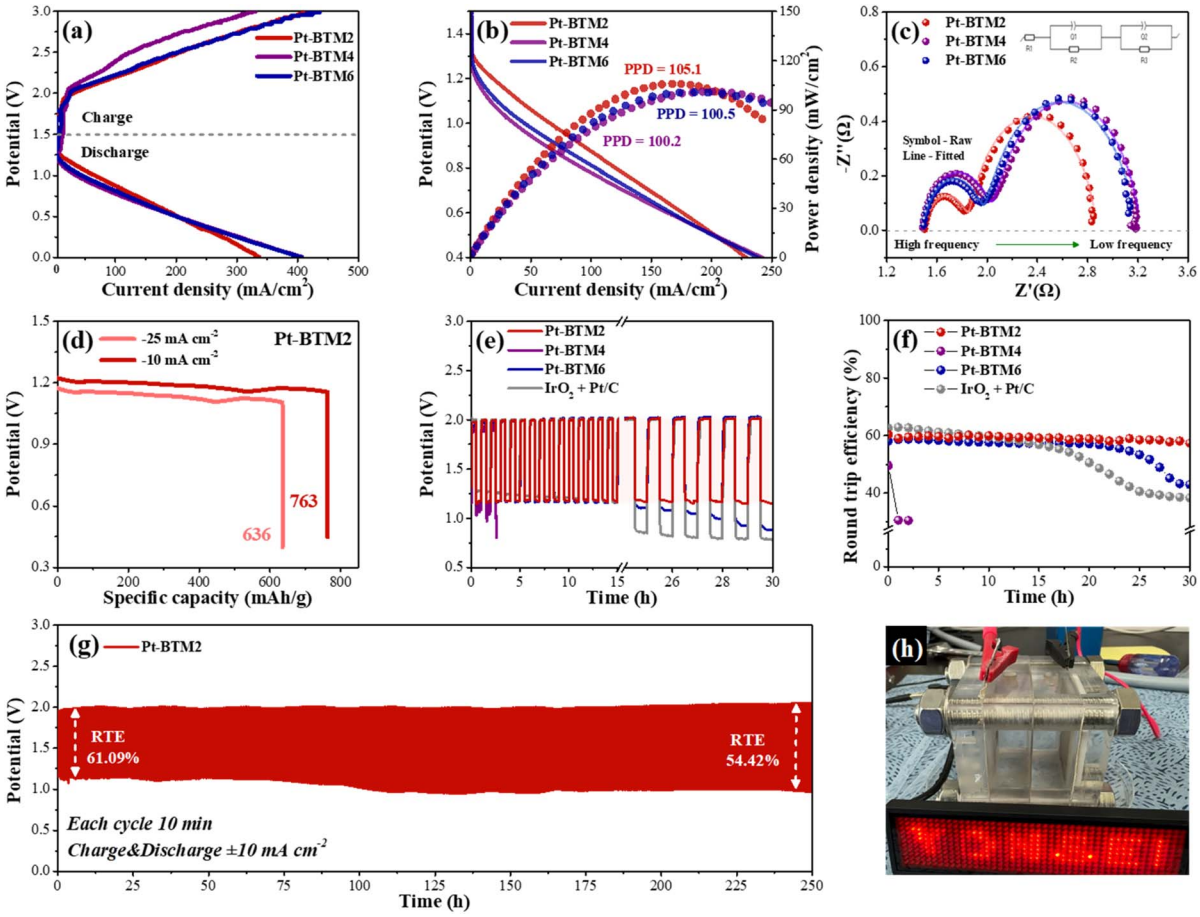

Fig. 5 Oxygen catalyst performance of the air cathode electrode of rechargeable ZABs: (a) charge and discharge polarization curves, and (b) discharge I–V–P polarization curves. (c) EIS spectra at 1 V. (d) Specific capacity of Pt-BTM2 at a discharge current density of −25 mA cm^{-2} and -10 mA cm^{-2}. (e) Galvanostatic charge–discharge cycling long-term stability of rechargeable ZABs, and the (f) RTE efficiency obtained from (e). (g) Pt-BTM2 galvanostatic charge–discharge cycling short-term stability of rechargeable ZABs. (h) Photographic image of a ZAB powering an LED screen.

demonstrates enhanced and differential activities in comparison to BTM*x*, even at a low level of Pt. Particularly, the strong synergistic interaction between Pt and the perovskite surface led to a remarkably greater enhancement in the ORR as compared to the OER. Of particular note is Pt-BTM2, which exhibited a superior and lowest bifunctionality of $\Delta E = 1.02$ V, accompanied by a substantial enhancement in its ORR activity from the additional synergistic reaction pathway between Pt and hexagonal BTM2 during the ORR process.

Zn–air battery performance

The application of the Zn–air batteries (ZABs) was performed using Pt-BTM*x* as air cathode electrode catalysts under an ambient atmosphere at room temperature. The galvanostatic charge and discharge polarization curves, illustrated in Fig. 5(a), demonstrate that the region above approximately 1.5 V corresponds to the charge region, while the region below corresponds to the discharge region where the OER and ORR occurred, respectively. The voltage gap between these charge and discharge steps reflects the overall overpotential, and thus the round-trip efficiency of the ZABs. Pt-BTM2 and Pt-BTM6 exhibited a higher current density compared to the Pt-BTM4 catalyst at the OER region.

As expected, the Pt-BTM2 catalyst showed relatively enhanced current density at the discharge region. For analysis of this discharge activity, the galvanostatic discharge *I–V–P* polarization curves are shown in Fig. 5(b). In comparing each of the Pt-BTM*x* catalysts, Pt-BTM2 exhibited the highest peak power density (PPD) with the order of Pt-BTM2; 105.1 mW cm^{-2} > Pt-BTM4; 100.2 mW cm^{-2} > Pt-BTM6; 100.5 mW cm^{-2}, likely due to the stronger synergistic coupling between Pt and the structurally stable hexagonal single-phase perovskite, which facilitates more efficient charge transfer during the ORR process.

To further investigate the resistance characteristic at this region, EIS was conducted at 1 V, and the fitted data was obtained using the equivalent circuit by $R_1(Q_1/R_2)(Q_2/R_3)$, as shown in Fig. 5(c). The fitted data for R_1, R_2, and R_3 correspond to R_s, R_{int} and R_{ct}, which denote contact and electrolyte resistance, solid–electrolyte interface resistance, and charge-transfer resistance, respectively. From the performance results, it was predictable that the Pt-BTM2 catalyst exhibited the smallest semicircle of the R_{ct} among the Pt-BTM*x* catalysts, with the resistance of 1.01 Ω, as summarized in Table S4. Interestingly, the solid–electrolyte interface resistance was also a much smaller R_{int}, with the resistance of 0.36 Ω (0.57 Ω and 0.49 Ω for Pt-BTM4 and Pt-BTM6, respectively). This indicates that the stronger synergistic coupling also reduces the interfacial resistance at the solid–electrolyte interface at the full cell system of the ZABs, further enhancing the overall OER/ORR kinetics.

The specific capacity of the ZABs is an essential indicator of the energy storage capability of the system and stability of anode degradation. The ZABs employing the Pt-BTM*x* catalysts as cathodes exhibit distinct differences in discharge performance, as shown in Fig. 5(d) and S10. Among the samples, Pt-BTM2 exhibited the highest specific capacity, including 763 mA h g^{-1} at a discharge current density of −10 mA cm^{-2}, reflecting its optimized ORR activity and efficient utilization of active sites. However, Pt-BTM4 exhibited anomalously unstable behaviour with a significantly lower capacity of 341 mA h g^{-1} at −25 mA cm^{-2} during the discharge process, which was likely affected by its unstable mixed-phase crystal structure and less favorable interfacial interaction with Pt, which hindered effective catalytic performance during the discharge process.

The instability of Pt-BTM4 was also confirmed by the galvanostatic charge–discharge cycling long-term stability test, as displayed in Fig. 5(e), as compared to the commercial IrO_2 + Pt/C cathode. Similar to its low specific capacity, it was observed that Pt-BTM4 also exhibited poor cycle stability, as evidenced by a noticeable decrease in voltage during discharge prior to 3 h of operation. It was caused by the battery recharge (discharge to charge), which resulted in harsh oxidative potential damage to the less favorable ORR mixed-phase of Pt-BTM4 and the formation of a significantly greater impurity phase as compared to Pt-BTM2 during operation, as depicted from the post-XRD analysis in Fig. S11.

Pt-BTM2 exhibited highly stable cyclic durability by maintaining its narrowest gap of 0.84 V during 30 h, which was a much more optimal performance than that of Pt-BTM6 or IrO_2 + Pt/C, at 1.14 V and 1.22 V, respectively. These results can be converted to the calculated RTE (%) for each catalyst. As shown in Fig. 5(f), it is evident that Pt-BTM2 demonstrates superior cyclic stability in comparison to other catalysts, maintaining a high RTE from 60.34% initially to 58.90% after 30 h. It is also noteworthy that the amount of 5 wt% Pt loading on perovskite was found to be optimal compared to 8 wt%, not only for the intrinsic catalytic (Fig. S7), but also for the exceptional cycling activities in the ZAB cell, as illustrated in Fig. S12. In contrast, the initial RTE of Pt-BTM6 and IrO_2 + Pt/C was recorded at 58.03% and 62.67%, yet diminished finally to 43.02% and 38.39%, respectively, indicating poor durability for both.

To highlight the practical feasibility of the catalyst in a commercial-like system, Fig. 5(g and h) confirmed that ZABs incorporating the Pt-BTM2 catalyst can reliably power an LED display, confirming its excellent real-world performance, as evidenced by the photographic image. Moreover, this great performance was maintained with an outstanding long-term operational stability over a duration of 250 h and 1500 cycles under the short-term cycling test, without significant changes in crystal structure, as shown by the post-XRD results (Fig. S11). Notably, the cyclic durability of Pt-BTM2 as a ZAB cathode outperformed the recently reported noble and non-noble metal-perovskite-based electrocatalysts while it maintained its catalytic activity, as summarized in the benchmarking data in Table S5.

Overall, these observations provide strong evidence for a distinct structure–activity relationship. We found that the hexagonal BTM2 offers a stable single-phase support with a more favorable electronic structure and interfacial environment for Pt, promoting superior ORR/OER kinetics and improved charge-transfer efficiency. Consequently, this structural advantage translates into exceptional cycling durability and energy efficiency in ZAB performance.

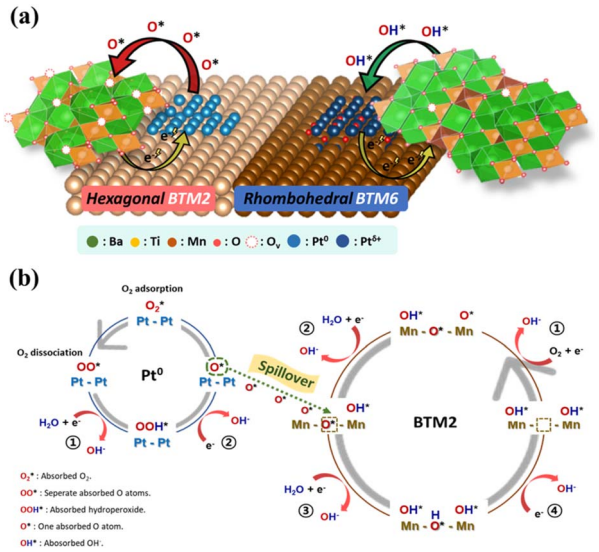

Fig. 6 Schematic illustration of the (a) Pt-BTM2 and Pt-BTM6 forming mechanism, and (b) the O* spillover mechanism on Pt-BTM2 during the ORR.

Bifunctional reaction mechanisms on Pt-BTM*x*

Considering the physical and electrochemical results discussed above, it was confirmed that Pt-BTM2 and Pt-BTM6 possess distinct reaction pathways in Pt-perovskite interactions, each governed by affected structural variations, which subsequently influence their bifunctional reaction, as illustrated in Fig. 6(a).

Under the suggested reaction mechanism in Fig. 6(b), it was hypothesised that Pt-BTM2 would be constructed through electron transfer from the oxygen species in perovskite to the loaded Pt, resulting in the appearance of oxidised O_2^{2-}/O^- and reduced Pt^0. During the ORR process, the presence of metallic Pt^0 and oxygen vacancies facilitated efficient reaction kinetics, and its catalytic activity was co-reacted by the O* spillover pathway. The reducing step of the O* molecule is an endothermic reaction, and is considered as the rate-determining step (RDS) on metallic Pt^0, and the adsorbed O* species can spill over to the oxygen vacancies on the perovskite surface, thereby facilitating its subsequent reduction.[25] This behaviour would likely be improved over the conventional four-electron ORR pathway in perovskites.

We suggest that the adsorption and dissociation of oxygen molecules occurred on the surface of the metallic Pt, and the dissociated OO* was consumed by forming OOH* and subsequently O* intermediates. Finally, the excess O* species then spilled over into neighboring oxygen vacancies within the perovskite BTM2 lattice. This effect between the Pt metal and the perovskite originates from the phenomenon of enhanced electron transfer and the formation energy of oxygen vacancies on the perovskite.[25,26] This synergy reduces the kinetic barriers and also contributes to the resistance to performance degradation, such as the oxidation of Pt during ORR operation.

Conversely, Pt-BTM6 operates *via* a different pathway, in which electrons are transferred from Pt to the perovskite surface. In the Pt-BTM6 catalyst system, the highest proportion of ionic $Pt^{\delta+}$ and reduced Mn^{3+} was observed, which is typically the favored species during OER.[24,33] Subsequently, the mechanism between ionic $Pt^{\delta+}$ and reducible metal (Mn^{3+}/Mn^{4+}) can be discussed, as illustrated in Fig. S13. The presence of a reducible metal species in the perovskite lattice can facilitate the binding of OH* and ionic Pt species, which appears *via* synergistic activities through the excess OH* spillover from the perovskite surface to the activated Pt sites, thereby enhancing the OER activity. The rhombohedral Pt-BTM6 follows a distinct pathway that favors OER kinetics, but provides less benefit to ORR stability.

Overall, we found that the catalytic activity and stability of the ORR reaction during the discharge process at the air cathode predominantly influence the application of air-cathodes in ZABs, emphasizing the importance of a robust ORR-active electrocatalyst. The combined physical, electrochemical, and mechanistic analyses confirmed that the hexagonal Pt-BTM2 catalyst enhanced the activity and stability by the aforementioned ORR mechanism through a stable single-phase support and unique synergistic interaction between metallic Pt^0 and the oxygen-defective perovskite surface. Consequently, the hexagonal Pt-BTM2 catalyst offers an optimal structure–activity correlation for reversible oxygen electrochemistry, enabling high round-trip efficiency and cycling stability in ZABs. Therefore, the present study highlights the critical role of composite structure engineering for an effective bifunctional oxygen catalyst, and provides key insights for the future development of practical metal–air energy storage systems.

Conclusions

In this study, we explored the potential for the adoption of a Pt-loaded barium titanate-based perovskite composite as a bifunctional oxygen catalyst. It is imperative to regulate the doping level of Mn to substitute B-site titanium, as this can result in adjustments to its crystal structure. This resulted in a consequential effect on the oxidation state of the surface of Pt. Hexagonal Pt-BTM2 exhibited a high concentration of oxygen vacancies and metallic Pt, which can be generated by electron transfer interaction (BTM2 to Pt). In contrast, rhombohedral Pt-BTM6 demonstrated an abundance of lattice oxygen and ionic platinum. It is evident that there are distinct interactions between Pt and perovskite, as well as varied pathways for the ORR and OER for each electrocatalyst.

Among these, the hexagonal Pt-BTM2 catalyst-based cathode demonstrated remarkable performance and stability during a cyclic charge–discharge test, with 1500 cycles and 250 h, thus establishing its efficacy as a bifunctional oxygen catalyst for rechargeable Zn–air batteries. Therefore, we can conclude that variations in crystal structure are a pivotal factor in determining catalytic behaviour when the material interacts with Pt. This structural influence has a significant impact on the bifunctional reaction pathway at the air cathode, ultimately enabling high-performance and durable bifunctional oxygen catalysts for next-generation rechargeable Zn–air batteries.

Author contributions

B. Kim: investigation, project administration, formal analysis, visualization, writing – original draft, data curation, K. Han: software, data curation, Y. Ko: visualization, writing – review and editing, C. Lee: funding acquisition, resources, writing – review and editing, Y. Jeon: conceptualization, supervision, project administration, writing – review and editing.

Conflicts of interest

There are no conflicts to declare.

Data availability

The data supporting this article have been included as part of the supplementary information (SI). Supplementary information: Fig. S1–S13 and Tables S1–S5. See DOI: https://doi.org/10.1039/d6ta00988c.

Acknowledgements

This work was supported by the Korea Institute of Energy Technology Evaluation and Planning (KETEP) and the Ministry of Trade, Industry & Energy (MOTIE) of the Republic of Korea (No. RS-2025-02310648).

Notes and references

1 E. Fabbri, A. Habereder, K. Waltar, R. Kötz and T. J. Schmidt, *Catal. Sci. Technol.*, 2014, **4**, 3800–3821.
2 W. T. Hong, M. Risch, K. A. Stoerzinger, A. Grimaud, J. Suntivich and Y. Shao-Horn, *Energy Environ. Sci.*, 2015, **8**, 1404–1427.
3 Z.-L. Wang, D. Xu, J.-J. Xu and X.-B. Zhang, *Chem. Soc. Rev.*, 2014, **43**, 7746–7786.
4 Y. Li and J. Lu, *ACS Energy Lett.*, 2017, **2**, 1370–1377.
5 H. Arandiyan, S. S. Mofarah, C. C. Sorrell, E. Doustkhah, B. Sajjadi, D. Hao, Y. Wang, H. Sun, B.-J. Ni and M. Rezaei, *Chem. Soc. Rev.*, 2021, **50**, 10116–10211.
6 S. Qin, K. Li, M. Cao, W. Liu, Z. Huang, G. He, I. P. Parkin and H. Li, *Nano Res. Energy*, 2024, **3**, e9120122.
7 K. W. Leong, Y. Wang, M. Ni, W. Pan, S. Luo and D. Y. Leung, *Renew. Sustain. Energy Rev.*, 2022, **154**, 111771.
8 J. Suntivich, K. J. May, H. A. Gasteiger, J. B. Goodenough and Y. Shao-Horn, *Science*, 2011, **334**, 1383–1385.
9 C. E. Beall, E. Fabbri and T. J. Schmidt, *ACS Catal.*, 2021, **11**, 3094–3114.
10 Y. Liu, S. Liu, P. Zhang, J. Zhou, H. Liu, S. Li, X. Li, X. Wang, D. Han and Y. Chen, *Adv. Funct. Mater.*, 2024, **34**, 2400522.
11 Y. Wei, Z. Weng, L. Guo, L. An, J. Yin, S. Sun, P. Da, R. Wang, P. Xi and C. H. Yan, *Small Methods*, 2021, **5**, 2100012.
12 X. Xu, W. Wang, W. Zhou and Z. Shao, *Small Methods*, 2018, **2**, 1800071.
13 J.-W. Zhao, Y. Li, D. Luan and X. W. Lou, *Sci. Adv.*, 2024, **10**, eadq4696.
14 K. Tewatia, A. Sharma, M. Sharma and A. Kumar, *Mater. Today: Proc.*, 2021, **44**, 4548–4556.
15 Y. Yang, Y. Zhou, J. Ren, Q. Zheng, K. H. Lam and D. Lin, *J. Am. Ceram. Soc.*, 2018, **101**, 2594–2605.
16 C.-F. Chen, G. King, R. M. Dickerson, P. A. Papin, S. Gupta, W. R. Kellogg and G. Wu, *Nano Energy*, 2015, **13**, 423–432.
17 S. M. Rahman, S. T. Norberg, C. S. Knee, J. J. Biendicho, S. Hull and S. G. Eriksson, *Dalton Trans.*, 2014, **43**, 15055–15064.
18 N. Tyminska, G. Wu and M. Dupuis, *J. Phys. Chem. C*, 2017, **121**, 8378–8389.
19 P. Xie, F. Yang, R. Li, C. Ai, C. Lin and S. Lin, *Int. J. Hydrogen Energy*, 2019, **44**, 11695–11704.
20 M. A. Rahman, Z. Hasan, J. Islam, D. Das, F. I. Chowdhury, M. U. Khandaker, H. M. Zabed, D. Bradley, H. Osman and M. H. Ullah, *ECS J. Solid State Sci. Technol.*, 2023, **12**, 103015.
21 G. Chen, Y. Ji, X. Shi, P. An, J. Zhang, Y. Li, S. F. Liu and J. Yan, *Chem. Eng. J.*, 2024, **496**, 154261.
22 M. Khalid, M. Y. Shah, N. Akbar, M. A. Masood, A. Nazar, B. Zhu, R. Raza and W. Jun, *Ceram. Int.*, 2024, **50**, 35734–35745.
23 Y. Zhu, C. Su, X. Xu, W. Zhou, R. Ran and Z. Shao, *Chem. – Eur. J.*, 2014, **20**, 15533–15542.
24 X. Han, F. Cheng, T. Zhang, J. Yang, Y. Hu and J. Chen, *Adv. Mater.*, 2014, **26**, 2047–2051.
25 W. Li, V. Drozd, M. S. I. Sozal, M. Li and Z. Cheng, *Solid State Ionics*, 2025, **421**, 116808.
26 X. Wang, J. Sunarso, Q. Lu, Z. Zhou, J. Dai, D. Guan, W. Zhou and Z. Shao, *Adv. Energy Mater.*, 2020, **10**, 1903271.
27 C. M. Enoch, S. Ingavale, P. Marbaniang, I. Patil and A. Swami, *J. Mater. Chem. A*, 2023, **11**, 21780–21792.
28 Y. C. Wu, S. F. Wang and S. H. Chen, *J. Am. Ceram. Soc.*, 2009, **92**, 2099–2108.
29 F. Ahmad, M. S. Lassoued, W.-P. Chen, G.-Y. Gou and Y.-Z. Zheng, *ACS Appl. Mater. Interfaces*, 2024, **16**, 31067–31075.
30 W. Xia, K. Leng, Q. Tang, L. Yang, Y. Xie, Z. Wu, K. Yi and X. Zhu, *J. Alloys Compd.*, 2021, **867**, 158808.
31 D. Zhen, B. Zhao, H. C. Shin, Y. Bu, Y. Ding, G. He and M. Liu, *Adv. Mater. Interfaces*, 2017, **4**, 1700146.
32 D. U. Lee, B. J. Kim and Z. Chen, *J. Mater. Chem. A*, 2013, **1**, 4754–4762.
33 X. Cao, Z. Tan, C. Ji and C. Pan, *Comput. Theor. Chem.*, 2025, **1244**, 115020.

